Nano Research
2022, 15(3): 2697–2705

ISSN 1998-0124 CN 11-5974/O4
https://doi.org/10.1007/s12274-021-3801-5

Research Article

Cs_2TiI_6: A potential lead-free all-inorganic perovskite material for ultrahigh-performance photovoltaic cells and alpha-particle detection

Peng Zhao[1,§], Jie Su[1,§], Yujia Guo[1], Lu Wang[1], Zhenhua Lin[1], Yue Hao[1], Xiaoping Ouyang[1,2,3], and Jingjing Chang[1] (✉)

[1] *State Key Discipline Laboratory of Wide Band Gap Semiconductor Technology, Shaanxi Joint Key Laboratory of Graphene, School of Microelectronics, Xidian University, 2 South Taibai Road, Xi'an 710071, China*
[2] *Shaanxi Engineering Research Center of Controllable Neutron Source, School of Science, Xijing University, Xi'an 710123, China*
[3] *State Key Laboratory of Intense Pulsed Radiation Simulation and Effect, Northwest Institute of Nuclear Technology, Xi'an 710024, China*
[§] *Peng Zhao and Jie Su contributed equally to this work.*

Received: 9 May 2021 / **Revised:** 26 July 2021 / **Accepted:** 8 August 2021

ABSTRACT

The lead contamination and long-term stability are the two important problems limiting the commercialization of organic–inorganic lead halide perovskites. In this study, through an innovative multi-scale simulation strategy based on the first-principle calculations coupling with drift-diffusion model and Monte Carlo method, a new discovery is shed on the vacancy-ordered double perovskite Cs_2TiI_6, a potential nontoxic and stable perovskite material for high-performance solar cell and α-particle detection. The excellent photon absorption character and ultrahigh carrier mobility (μ_n = 2.26×10^4 cm^2/Vs, μ_p = 7.38×10^3 cm^2/Vs) of Cs_2TiI_6 induce ultrahigh power conversion efficiency (PCE) for both single-junction solar cell (22.70%) and monolithic all-perovskite tandem solar cell (26.87%). Moreover, the outstanding device performance can be remained even in high energy charge particle detection (α-particle) with excellent charge collection efficiency (CCE = 99.2%) and mobility-lifetime product ($\mu\tau_h$ = 1×10^{-3} cm^2/V). Furthermore, to our surprise, the solar cell and α-particle detector based on Cs_2TiI_6 material are able to withstand ultrahigh fluence proton beam up to 10^{13} and 10^{15} p/cm^2 respectively, which strongly suggests that semiconductor devices based on Cs_2TiI_6 material are able to apply in the astrospace. The multi-scale simulation connecting from material to device reveals that Cs_2TiI_6 perovskite has the great potential for photovoltaic cells, α-particle detection and even their space application.

KEYWORDS

Cs_2TiI_6, first-principle theory, drift-diffusion model, Monte Carlo method, alpha-particle detection

1 Introduction

Halide perovskites have attracted tremendous research attention due to the long electron-hole diffusion length, high carrier mobility, large average atomic number, high absorption coefficient, and high photoluminescence quantum yield [1–4]. Benefiting from these excellent optoelectronic properties, halide perovskites could be widely used in solar cells [1], light emitting diodes [2], photodetectors [3], lasers [4], field effect transistors [5], thermoelectrics [6], X-ray detection [7], α-particle detection [8], etc. Due to the advantages of excellent photoelectric characters, mechanical flexibility and light weight, perovskite solar cells exhibit the great potential for space application, such as space station, spacecraft and satellites. In the space environment, the performance of solar cells will deteriorate due to the existence of high energy cosmic particles such as proton. According to the previous research, perovskite solar cells can withstand proton irradiation up to about 10^{12}–10^{13} p/cm^2 [9–13]. Moreover, in 2017, halide perovskite was firstly used in α-particle detection by employing $MAPbBr_3$ single crystal with high $\mu\tau_h$ value of (0.4–1.6) × 10^{-3} cm^2/V [8]. However, the environment-unfriendly and toxic Pb component and the hygroscopic and volatile organic cations have limited the commercial application of the halide perovskite [14–17]. Therefore, it is necessary to explore the stable lead-free all-inorganic halide perovskite to overcome these shortcomings. According to previous reports, cesium cation (Cs^+) could be used to replace MA^+ and FA^+, which remarkably improved the moisture and thermal stability [18]. Meanwhile, the toxicity Pb^{2+} could be replaced by one kind of nontoxicity cations, including silver (Ag^+), indium (In^+), antimony (Sb^{3+}), bismuth (Bi^{3+}), germanium (Ge^{2+}) and tin (Sn^{2+}) [19–23]. In 2017, Greul et al. applied $Cs_2AgBiBr_6$ into solar cells for the first time with a PCE of 2.43% and a V_{oc} exceeding 1 V [24]. After that, Gao et al. prepared the high-quality, ultra-smooth $Cs_2AgBiBr_6$ thin film with high crystallinity by employing anti-solvent dropping and post-annealing strategy, and the photovoltaic cell based on $Cs_2AgBiBr_6$ exhibited a PCE of up to 2.23% with no hysteresis [25]. However, the wide band gap of $Cs_2AgBiBr_6$ impedes the further improvement of device performance. In addition to the commonly used $Cs_2AgBiBr_6$, the vacancy-ordered double

Address correspondence to jjingchang@xidian.edu.cn

perovskite Cs_2SnI_6 was employed as the active layer owing to its suitable band gap (1.48 eV) by Qiu et al. [26]. However, the low PCE (< 1%), the intrinsically deep defects, and unsatisfactory stability impede the further development of Cs_2SnI_6 photovoltaic cells. Afterwards, Cs_2TiBr_6 thin-films prepared with the low-temperature vapor based method was incorporated into perovskite solar cells by Chen et al. [27] who reported a PCE of 3.28% and superior intrinsic environmental stability. However, the PCE of Cs_2TiBr_6 solar cells is still low. Therefore, it is necessary to explore new lead-free all-inorganic perovskites with excellent device performance. In addition, zero-dimensional lead-free all-inorganic perovskite $Cs_3Bi_2I_9$ and $Rb_3Bi_2I_9$ single crystals have been synthesized by McCall et al. and applied to α-particle detection. Similarly, the ultra-low $\mu\tau_h$ value ($Cs_3Bi_2I_9$: 1.8×10^{-5} cm²/V, $Rb_3Bi_2I_9$: 2×10^{-6} cm²/V) greatly limits their further development [28].

Herein, a novel vacancy-ordered double perovskite Cs_2TiI_6 which is free of organic molecules and lead is discovered. Meanwhile, the suitability of the novel perovskite material for application in photovoltaic cells and α-particle detection is investigated by combining first principles calculation with drift diffusion theory and Monte Carlo method. According to the results, an ultrahigh PCE (22.7%) of Cs_2TiI_6 photovoltaic cells can be obtained and it can survive against accumulated dose levels up to 1×10^{13} p.cm^{-2} of protons irradiation. Furthermore, vacancy-ordered double perovskite Cs_2TiI_6 is used for α-particle detection and the high $\mu\tau_h$ product (1×10^{-3} cm²/V) and CCE (99.2%) are realized. Overall, Cs_2TiI_6 exhibits great potential in photovoltaic cells and radiation detection.

2 Method

First-principle calculation: Density functional theory (DFT) is adopted for the first principles calculation by the projector augmented wave (PAW) method as implemented in the VASP code [29]. Generalized gradient approximation (GGA) with Perdew–Burke–Ernzerhof (PBE) functional is employed [30]. The plane-wave cutoff energy is set to be 500 eV. A 7×7×7 k-point grid is adopted. All structures are fully relaxed until the total energies and maximum residual force are converged up to 10^{-5} eV and 0.005 eV/Å, respectively. To reasonably obtain the optoelectronic properties, the hybrid density functional method based on the Heyd-Scuseria-Ernzerhof (HSE) scheme with 0.05 Hartree-Fock exchange energy is considered after extensive test. The transport parameters of Cs_2TiI_6 are obtained by the following equations

$$\frac{1}{m^*} = \frac{1}{(h/2\pi)^2}\frac{\mathrm{d}^2E}{\mathrm{d}k^2} \tag{1}$$

$$N_C = 2\frac{(2\pi m_n^* k_0 T)^{3/2}}{h^3}, N_V = 2\frac{(2\pi m_p^* k_0 T)^{3/2}}{h^3} \tag{2}$$

$$\mu_\beta^{3D} = \frac{2\sqrt{2\pi}eC_\beta^{3D}\hbar^4}{3(k_0T)^{3/2}E_\beta^2 m^{*5/2}} \tag{3}$$

$$E_\beta = \frac{\Delta V}{\Delta l/l_0} \tag{4}$$

$$C_\beta^{3D} = \frac{1}{V_0}\frac{\partial^2 E}{\partial(\Delta l/l_0)^2} \tag{5}$$

where m^* is the effective mass,h is Planck's constant, k_0 is Boltzmann's constant, T is the temperature, E_β is deformation potential (DP) constant, ΔV is the energy change of the conduction band minimum and valence band maximum, $\Delta l/l_0$ is lattice dilation along the direction of β, C_β^{3D} is 3D elastic constant, V_0 is volume of unit cell, N_c is effective conduction band density, N_v is effective valence band density, and μ_β^{3D} is carrier mobility.

Drift-diffusion model: The drift-diffusion equation (Eq. (6)), carrier continuity equation (Eq. (8)) and Possion's equation (Eq. (7)) are adopted. Transfer-matrix method (TMM) is used to calculate carrier generation rate (Eq. (9)), where $Q(x, \lambda)$ is absorption energy per unit area and $E(x)^2$ is optical electric field. Standard AM 1.5G solar spectrum is employed to act as sunlight, and Shockley-Read-Hall recombination is considered in the device. Such method has been proven to be suitable for perovskite solar cells [31–35]. For α-particle detection, the carrier generation rate is computed by energy deposition obtained from Stoping Range of Ions in Matter (SRIM) [36]. The material parameters of Cs_2TiI_6 are obtained from the first-principle calculations and literatures, as listed in Tables S1 and S2 in the ESM [37–44].

$$J_n = qD_n\frac{\partial n}{\partial lx} - q\mu_n n\frac{\partial\phi}{\partial x}, J_p = -qD_p\frac{\partial p}{\partial x} - q\mu_p n\frac{\partial\phi}{\partial x} \tag{6}$$

$$\frac{\partial^2\phi}{\partial x^2} = \frac{q}{\varepsilon}(n-p) \tag{7}$$

$$\frac{\partial n}{\partial t} = \frac{1}{q}\frac{\partial J_n}{\partial x} + G - R, \frac{\partial p}{\partial t} = \frac{1}{q}\frac{\partial J_p}{\partial x} + G - R \tag{8}$$

$$Q(x,\chi) = \frac{2\pi c\varepsilon_0 kn|E(x)|^2}{\chi} \tag{9}$$

Monte Carlo method: To simulate the radiation effect, the SRIM 2013 program based on Monte Carlo method is employed with a total of 10^6 incident ions. Detailed calculation with full damage is considered in this simulation. The material densities are: ρ_{Ag}=10.49 g/cm³, $\rho_{C_{60}}$=1.65 g/cm³, ρ_{MAPbI_3}=4.118 g/cm³, $\rho_{PEDOT:PSS}$=1.475 g/cm³, $\rho_{Cs_2TiI_6}$=5.238 g/cm³, ρ_{FTO}=6.99 g/cm³, ρ_{Glass}=2.32 g/cm³.

3 Results and discussion

The crystal structure of vacancy-ordered double perovskite Cs_2TiI_6 is displayed in Fig. 1(a) with $Fm3m$ space group. The lattice parameter of Cs_2TiI_6 of about 11.09 Å is in good agreement with the previous report [45]. The band structure calculated by two different methods (PBE and HSE) is shown in Fig. 1(b). Compared to the band gap obtained by the PBE method (0.65 eV), the HSE method gives a direct band gap of about 1.02 eV for Cs_2TiI_6, which is close to that of Si (1.12 eV). Similar to the $MAPbI_3$, the conduction band minimum (CBM) and the valence band maximum (VBM) are mainly composed of the d orbital of Ti atom and the p orbital of I atom, respectively, as shown in Fig. 1(c). The calculated electron mobility (2.26×10^4 cm²/Vs) and hole mobility (7.38×10^3 cm²/Vs) are significantly superior to those of $MAPbI_3$ due to the larger elastic constant C_β^{3D} and smaller deformation potential constant E_β, as listed in Figs. 1(d)–1(f) and Table S2 in the ESM [39,44]. Meanwhile, the Cs_2TiI_6 exciton binding energy (E_b) which qualitatively represents the photo-generation carrier recombination is comparable with that of $MAPbI_3$, as demonstrated in Fig. 1(f). The detailed E_b of Cs_2TiI_6 is calculated by Bethe-Salpeter equation $E_b=\mu^*R_y/m_0\varepsilon_r^2$, where μ^* is reduced effective mass ($1/\mu^*=1/m_n^*+1/m_p^*$), R_y is the atomic Rydberg energy, and ε_r is relative dielectric constant. The excellent carrier mobility and comparable exciton binding energy suggest that Cs_2TiI_6 may possess a greater potential than $MAPbI_3$ in the application of photovoltaic cells and radiation detection. To

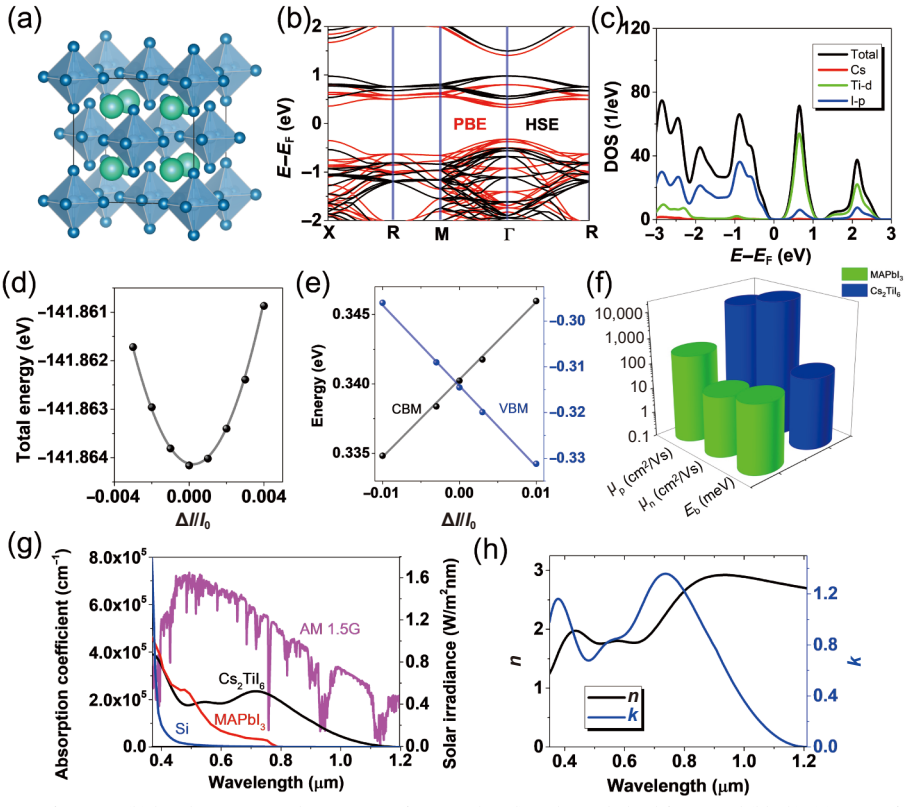

Figure 1 (a) Crystal structure of Cs_2TiI_6; (b) band structure with GGA-PBE functional (red) and HSE hybrid functional (black); (c) DOS of Cs_2TiI_6; (d) total energy of Cs_2TiI_6 as a function of lattice dilation; (e) CBM and VBM of Cs_2TiI_6 as a function of lattice dilation; (f) exciton binding energy and carrier mobility of Cs_2TiI_6 and $MAPbI_3$; (g) solar spectrum and absorption coefficients of Cs_2TiI_6, $MAPbI_3$, and Si; (h) refractive index n and extinction coefficient k of Cs_2TiI_6.

further unveil the optoelectronic application of Cs_2TiI_6, the absorption coefficient of Cs_2TiI_6 coupling with the solar spectrum of AM 1.5G is displayed in Fig. 1(g). The absorption coefficient of Cs_2TiI_6 in the entire solar spectrum is up to 10^5 cm^{-1}. Moreover, such absorption coefficient is significantly superior to that of Si in the entire-wavelength region and $MAPbI_3$ in long-wavelength region. It suggests Cs_2TiI_6 can absorb the larger proportion of solar spectrum than $MAPbI_3$ and Si. In other words, the vacancy-ordered double perovskite Cs_2TiI_6 may possess the great potential to be applied in photovoltaic cells. Inspired by these excellent optoelectronic properties above mentioned, the vacancy-ordered double perovskite Cs_2TiI_6 possesses broad prospect for the application in solar cells and radiation detection.

In order to assess Cs_2TiI_6 as a potential photovoltaic and radiation material, a multi-scale simulation strategy is employed to investigate the device performance based on Cs_2TiI_6 material. The detailed optical and transport characters are calculated and displayed in Figs. 1(g) and 1(h) and Table S2 in the ESM, which is then transferred to transfer-matrix method and drift-diffusion model and Monte Carlo method for further analysis of solar cell and α-particle detection.

The widely adopted solar cell structure (FTO/PEDOT:PSS/Cs_2TiI_6/C_{60}/Ag) is employed in the simulation by combining transfer-matrix method with drift-diffusion model. As shown in Fig. 2(a), with the Cs_2TiI_6 thickness increase, the short circuit current density (J_{sc}) rapidly increases from 18.89 to 39.53 mA/cm² when the perovskite thickness is less than 50 nm. After that, the J_{sc} demonstrates an evident oscillation phenomenon with three peaks

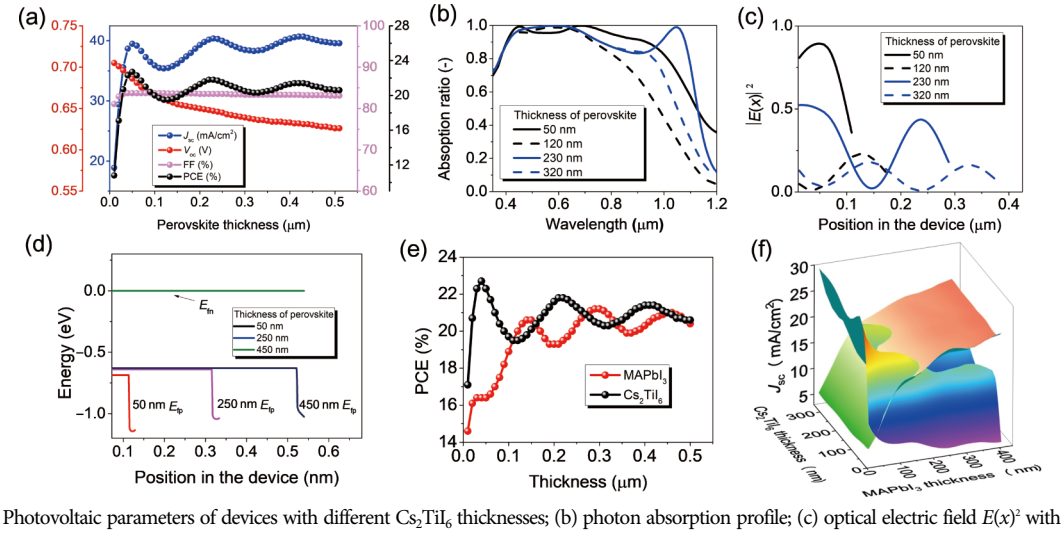

Figure 2 (a) Photovoltaic parameters of devices with different Cs_2TiI_6 thicknesses; (b) photon absorption profile; (c) optical electric field $E(x)^2$ with the wavelength of 1050 nm; (d) Quasi Fermi levels of the device under open-circuit condition; (e) dependence of PCE of $MAPbI_3$ (red) and Cs_2TiI_6 (black) on the thickness of the materials; (f) current matching of monolithic Cs_2TiI_6-$MAPbI_3$ tandem solar cell.

and two valleys. The corresponding Cs_2TiI_6 thicknesses of the three peaks are 50, 230, and 420 nm, and those of the two valleys are 120 and 320 nm, respectively. The oscillation phenomenon can be illustrated by photon absorption profile displayed in Fig. 2(b). When the incident light is in short-wavelength region, the refractive index of Cs_2TiI_6 is well matched to the nearby carrier transport layer and transparent electrode, which results in a lower reflection and interference loss [46]. Consequently, the lights in the short-wavelength are fully abosrbed, irrespective of the perovskite thickness. When the incident light locates in long-wavelength region, the unmatched refractive index may induce the higher reflection loss. Meanwhile, the increasing perovskite thickness may correspond to the multiple of wavelength which may induce strong interference loss (see Fig. S1 in the ESM), and then reduce the optical electric field $E(x)^2$, as illustrated Fig. 2(c). Thus, the absorption ratio of Cs_2TiI_6 in the long wavelength oscillates as the thickness increases. Taking the 1,050 nm wavelength light as examples, the optical electric field $E(x)^2$ with 50 nm perovskite layer is about 3.8 times higher than that with 120 nm perovskite layer (see Fig. 2(c)), therefore, the photon absorption ratio (55.9%) of 50 nm perovskite layer is about 3 times higher than that of 120 nm perovskite layer (17.3%). As a result, the more excellent electron-hole pair generation rate with 50 nm perovskite layer can be obtained, thus, the J_{sc} of device based on 50 nm perovskite layer is superior to that of device based on 120 nm perovskite layer. The similar situation can be observed for the 230 and 320 nm perovskite layer. Except for J_{sc}, the fill factor (FF) almost remains constant and the open circuit voltage (V_{oc}) keeps decreasing, as illustrated in Fig. 2(d), since the difference between electron quasi Fermi level and hole quasi Fermi level keeps dropping with the increment of perovskite thickness. In order to verify the excellent photoelectric characters of Cs_2TiI_6, the traditional $MAPbI_3$ solar cell is simulated with the same device structure as reference and shown in Fig. 2(e). The efficient absorption of Cs_2TiI_6 allows PCE to reach the first peak value (22.7%) in just 50 nm thickness which is 1.4 times higher than that of $MAPbI_3$ with the same thickness. Besides, all the three peak PCE values of Cs_2TiI_6 based devices (PCE: 22.7%, thickness: 50 nm; PCE: 21.8%, thickness: 230 nm; PCE: 21.4%, thickness: 420 nm) are superior to the highest peak PCE value of $MAPbI_3$ based device (PCE: 21.2%, thickness: 300 nm), which indicates that Cs_2TiI_6 is a kind of suitable materials for photovoltaic cells.

It should be noted that the above optimal performances of Cs_2TiI_6 solar cells are derived from the ideal natural physical parameters of the Cs_2TiI_6 single crystal. In the real experiment, the generally synthesized perovskite absorption layer is polycrystalline with lower carrier mobility and lifetime and larger defect states which determine the carrier recombination. As a result, the simulated optimal performance of the perovskite based device, such as the Cs_2TiBr_6 solar cell, may be far superior to the experimental value [27, 47]. Note that, all of the carrier mobility, lifetime, and defect states can be improved by enhancing the film quality of the perovskite. To realize the high-performance perovskite solar cell (PSC) based on Cs_2TiI_6, the PCEs dependent on the carrier mobility, lifetime and defect energy level are illustrated in Figs. S2 and S3 in the ESM. It can be found that when the carrier mobility is below 1 cm^2/Vs and continues to decreasing, the PCE significantly decreases from 22.7% to 1.1%, since the low carrier mobility accompanies with severely carrier recombination, as illustrated in Fig. S2 in the ESM. When the carrier mobility is higher than 1 cm^2/Vs, the PCE almost keeps a constant. It means that the high-performance PSC based on Cs_2TiI_6 can be achieved by enlarging the carrier mobility. In addition, with carrier lifetime enlarging from 10^{-10} to 10^{-6} s (which corresponds to the order of magnitude of Cs_2TiI_6 single crystal), the PCE (carrier recombination rate) almost linearly increases (decreases), and then tends to a saturation with further enlarging the carrier lifetime (see Fig. S3 in the ESM). In other words, enlarging the carrier lifetime of Cs_2TiI_6 polycrystalline film is an effective way to improve the performance of PSC based on Cs_2TiI_6. In addition, as shown in Fig. S4 in the ESM, the PCE can be improved when the defect energy level stays away from the intrinsic Fermi level, especially the distance is larger than 0.2 eV. Because the defect energy level could capture electrons and holes more efficiently when the defect energy level closes to the intrinsic Fermi level, which induces the larger recombination rate. Thus, tuning and enlarging the defect energy level is another way to realize the high-performance PSC based on Cs_2TiI_6. In general, all the carrier mobility, lifetime and defect energy level of perovskite can be improved by enhancing the film quality of perovskite in the experiment. Therefore, the high-performance PSC based on Cs_2TiI_6 may be realized by improving the crystal quality of Cs_2TiI_6 film with the large carrier mobility, lifetime and defect energy level.

Owing to the relatively narrow band gap of Cs_2TiI_6, the absorption cutoff can be up to about 1,200 nm, which indicates that Cs_2TiI_6 is suitable to be the bottom cell for tandem solar cells. The tandem structure of FTO/PEDOT:PSS/$MAPbI_3$/C_{60}/ITO/PEDOT:PSS/Cs_2TiI_6/C_{60}/Ag is used to investigate the performance of the monolithic all-perovskite tandem solar cell, as displayed in Fig. S5 in the ESM. Because the J_{sc} of the tandem solar cell is limited by the minimum one of all the sub-cells, it is necessary to explore the current matching of all–perovskite monolithic tandem solar cells. The current matching is shown in Fig. 2(f), and the intersection between both surfaces represents current matching points. Similar to the single junction solar cell, the oscillation phenomenon of J_{sc} is observed in the monolithic Cs_2TiI_6-$MAPbI_3$ tandem solar cell as well. To our surprise, both ultra-thin absorption layer thickness ($MAPbI_3$ = 186 nm, Cs_2TiI_6 = 70 nm) and excellent device performance (J_{sc} = 19.08 mA/cm^2, V_{oc} = 1.70 V, FF = 82.53%, PCE = 26.87%) can be obtained under the condition of optimal current matching, which is significantly superior to the reported highest PCE (24.8%) of all–perovskite monolithic tandem solar cells [48]. Therefore, vacancy-ordered double perovskite Cs_2TiI_6 is a potential lead-free all-inorganic perovskite material for both single junction solar cell and monolithic all–perovskite tandem solar cell.

Perovskite solar cells have exhibited great potential for space application. In order to explore the feasibility of the Cs_2TiI_6 solar cell in astrospace, the proton irradiation tolerance is necessary to be investigated. The proton beam with energy ranging from several keV to hundreds of MeV consists of positive hydrogen nucleus. In order to minimize the influence of glass substrate in proton penetration, the proton beam is irradiated from the Ag electrode. Nuclear scattering of the incident proton results in the target nuclei to recoil and be displaced, which instigates a cascade of damage events that generate vacancies in the material. The proton penetration and vacancies distribution with 50 nm champion perovskite thickness are calculated by Monte Carlo method using computer program SRIM 2013 and displayed in Fig. 3. It can be observed that the low-energy proton beam (5 keV) cannot reach active layer and the high-energy proton beam (1 MeV) mostly passes through the entire device without substantial collision event, only the moderate-energy proton beam (25 and 40 keV) induces evident collision events and vacancies in the active layer, suggesting that only the moderate-energy proton beam has a strong effect on the device performance. Furthermore, the vacancy concentration in the active layer induced by the 25 keV proton beam is higher than that induced by the 40 keV proton beam. It is thought that the 25 keV proton beam may induce the greatest

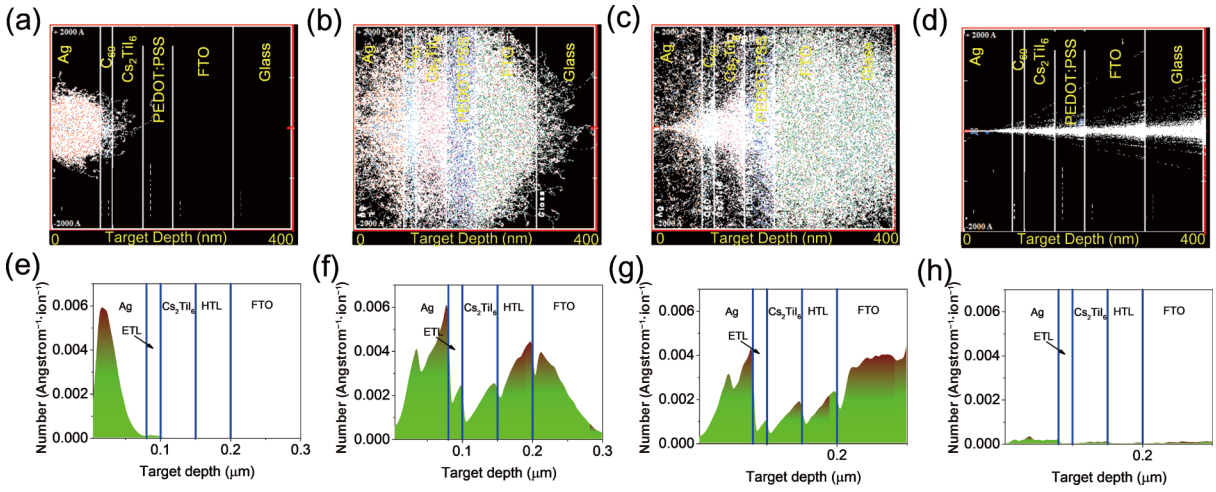

Figure 3 50 nm Cs_2TiI_6 layer: profile of (a) 5 keV, (b) 25 keV, (c) 40 keV, (d) 1 MeV proton penetration in the single junction Cs_2TiI_6 solar cell; the distribution of vacancies when the single junction Cs_2TiI_6 solar cell is bombarded by proton with energy of (e) 5 keV, (f) 25 keV, (g) 40 keV, (h) 1 MeV.

damage on the device and thus such proton beam is selected in the following discussion. In order to quantitatively analyze the deterioration of device performance induced by the proton irradiation, the drift-diffusion model coupling with the Monte Carlo method is employed. As shown in Fig. 4(a), the ultrahigh PCE, V_{oc}, J_{sc}, and FF of Cs_2TiI_6 solar cell under the AM1.5G and AM0 illumination without proton beam are 22.7%, 0.685 V, 39.5 mA/cm^2, 83.7% and 20.6%, 0.691 V, 48.6 mA/cm^2, 83.7%, respectively. This performance is much higher than the experimental results since a perfect crystal structure is considered in this work, which also indicates that the Cs_2TiI_6 still has much potential for further improvement. In Figs. 4(b) and 4(c), we found the Cs_2TiI_6 photovoltaic cell possesses the excellent radiation tolerance in the wide range of proton fluence. When the Cs_2TiI_6 solar cell undergoes 25 keV proton beam, the V_{oc} keeps remaining, and then V_{oc} gradually deteriorates when the proton fluence overs 10^{13} p/cm^2. This is because the 25 keV proton beam fluence below 10^{13} p/cm^2 is insufficient to increase the carrier recombination and tune the Fermi level, as seen in Figs. 4(d) and 4(e). When continueously increasing the proton fluence, the increasing carrier recombination rate leads to the decrease of photo-generated non-equilibrium carriers concentration, and then results in the decline of the difference between electron and hole quasi Fermi level, which induces the drop of V_{oc}, as illustrated in Figs. 4(d) and 4(e). For the excellent J_{sc} of Cs_2TiI_6 solar cell, it just slightly shifts down about 3.3 mA/cm^2 even though the proton fluence is up to 1×10^{16} p/cm^2, since the significant deterioration of EQE is observed just when the proton fluence is beyond 10^{16} p/cm^2. For an example, EQE with 1×10^{16} p/cm^2 proton irradiation in 700 nm wavelength is 0.971 which is comparable to that of Cs_2TiI_6 solar cell without proton irradiation, but is far higher than that with 2×10^{16} p/cm^2 (EQE = 0.243). In addition, the variation of FF under the proton irradiation is similar to that of J_{sc}. As a result, the Cs_2TiI_6 solar cell still retains over 95% of their initial PCE even after being irradiated by 25 keV proton beam at high-fluence of 10^{13} p/cm^2. Especially, the J_{sc} can withstand proton irradiation up to 10^{16} p/cm^2 without significant current loss. It means Cs_2TiI_6 solar cell exhibits an excellent proton resistance and great potential application in the astrospace.

In order to further explore the Cs_2TiI_6 space solar cell, other two solar cells with 230 and 420 nm perovskites coupling with $MAPbI_3$ solar cell under the greatest proton radiations are investigated, as shown in Figs. S6–S8 in the ESM, respectively. It can be found that the greatest tolerations of proton energy for 230 nm Cs_2TiI_6 solar cell and 420 nm Cs_2TiI_6 solar cell are 40 and 60 keV, respectively, which are higher than that of 50 nm Cs_2TiI_6 solar cell. As to the $MAPbI_3$ solar cell, its champion PCE corresponds to the 300 nm $MAPbI_3$ layer. The greatest toleration of proton energy for 300 nm $MAPbI_3$ solar cell is 35 keV (Fig. S8 in the ESM) which is obviously lower than that of corresponding Cs_2TiI_6 solar cell. In other words, the Cs_2TiI_6 solar cell can resist the higher proton energy than $MAPbI_3$ solar cell due to the larger mass density of

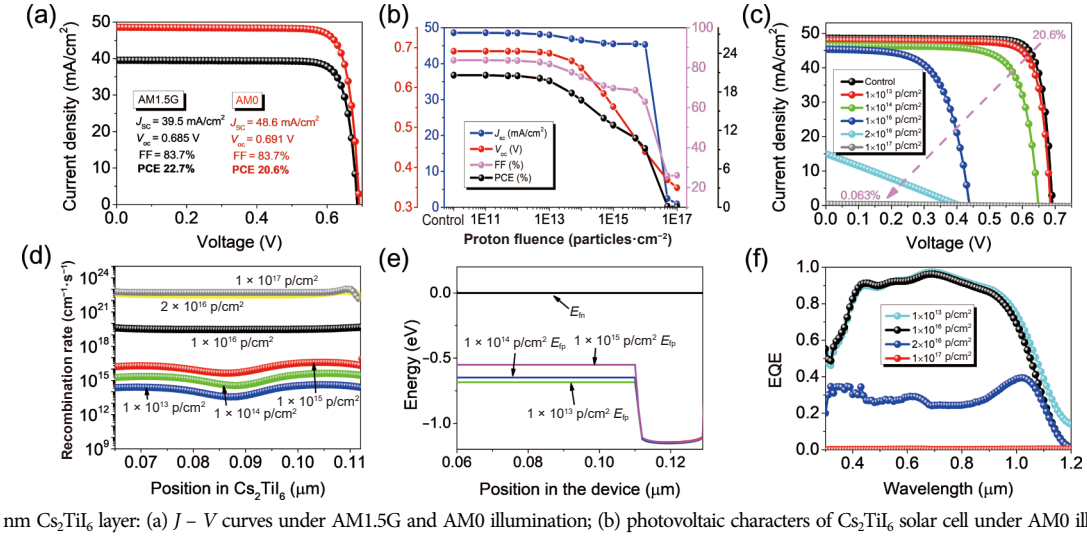

Figure 4 50 nm Cs_2TiI_6 layer: (a) $J-V$ curves under AM1.5G and AM0 illumination; (b) photovoltaic characters of Cs_2TiI_6 solar cell under AM0 illumination as a function of 25 KeV proton beam fluence; (c) $J-V$ curves, (d) recombination rate, (e) Quasi Fermi levels under open-circuit condition, and (f) EQE of the device with various proton fluences.

Cs_2TiI_6 (5.238 g/cm^3) than that of $MAPbI_3$ (4.118 g/cm^3). In addition, regardless of the thickness of Cs_2TiI_6, the Cs_2TiI_6 solar cell can at least tolerance 1×10^{13} p/cm^2 proton irradiation, while the $MAPbI_3$ solar cell can only resist 5×10^{12} p/cm^2 proton irradiation which is only half of Cs_2TiI_6 solar cell. These further suggest the more potential application of Cs_2TiI_6 solar cell in the astrospace. Table 1 comparatively lists the proton irradiation tolerances of reported solar cells and this work. To our surprise, Cs_2TiI_6 solar cell possesses the champion radiation resistance compared with the other perovskite solar cells and the traditional commercialized photovoltaic cells (Si, GaAs). The Si and GaAs solar cells can only resist the proton irradiation with 10^{11} and 10^{10} p/cm^2, respectively, which means that Cs_2TiI_6 solar cell has at least two to three orders of magnitude higher proton tolerance than Si and GaAs solar cells. In addition, the proton tolerance of both single junction and double junction perovskite solar cells reported in literatures is obviously worse than that of the Cs_2TiI_6 solar cell. Meanwhile, high-energy 68 MeV proton beam adopted in the literatures is too high to cause significant collision event, making correct assessment of proton tolerance difficult [11–13]. It is thought that the excellent radiation resistance of Cs_2TiI_6 solar cell is endowed by the nature of ultra-thin absorption layer, high carrier mobility, all of which can minimize the influence of radiation damage on photovoltaic performance. Therefore, the above analysis reveals that Cs_2TiI_6 solar cell is radiation hard and has broad prospects for space application.

Due to the excellent radiation tolerance of photovoltaic cells, Cs_2TiI_6 perovskite might have great potential for radiation detection. The widely adopted metal/Cs_2TiI_6/metal structure is used as α-particle detector with 5.48 meV α incident particles energy. As shown in Fig. 5(a), the incident depth of α-particle in Cs_2TiI_6 radiation detector is about 23.6 μm. With the α-particle penetrating deeper into the device, the velocity of particles declines owing to the loss of energy, and therefore, the cross section and

Table 1 Photovoltaic cells: the comparison of proton irradiation tolerance in this work and literatures

Device structure	Proton energy (keV)	Proton fluence (p/cm^2)	Ratio maintaining the initial performance (%)	Ref.
AZO/SnO_2/$Cs_{0.05}(MA_{0.17}FA_{0.83})_{0.95}Pb(I_{0.83}Br_{0.17})_3$/Spiro-OMeTAD/Au	150	10^{13}	80	[9]
ITO/PEDOT:PSS/$MAPbI_3$/PCBM/BCP/Ag	100	3×10^{12}	80	[10]
ITO/PEDOT:PSS/$MAPbI_3$/PCBM/Ag	68,000	10^{12}	90	[11]
ITO/PTAA/$Cs_{0.05}MA_{0.17}FA_{0.83}Pb(I_{0.83}Br_{0.17})_3$/$C_{60}$/BCP/Cu	68,000	10^{12}	95	[12]
Perovskite/CIGS tandem solar cell	68,000	2×10^{12}	85	[13]
Si solar cell	10,000	10^{11}	90	[49]
GaAs solar cell	150	10^{10}	88	[50]
FTO/PEDOT:PSS/Cs_2TiI_6/C_{60}/Ag	25/40/60	10^{13}	95	This work
FTO/PEDOT:PSS/$MAPbI_3$/C_{60}/Ag	35	5×10^{12}	95	This work

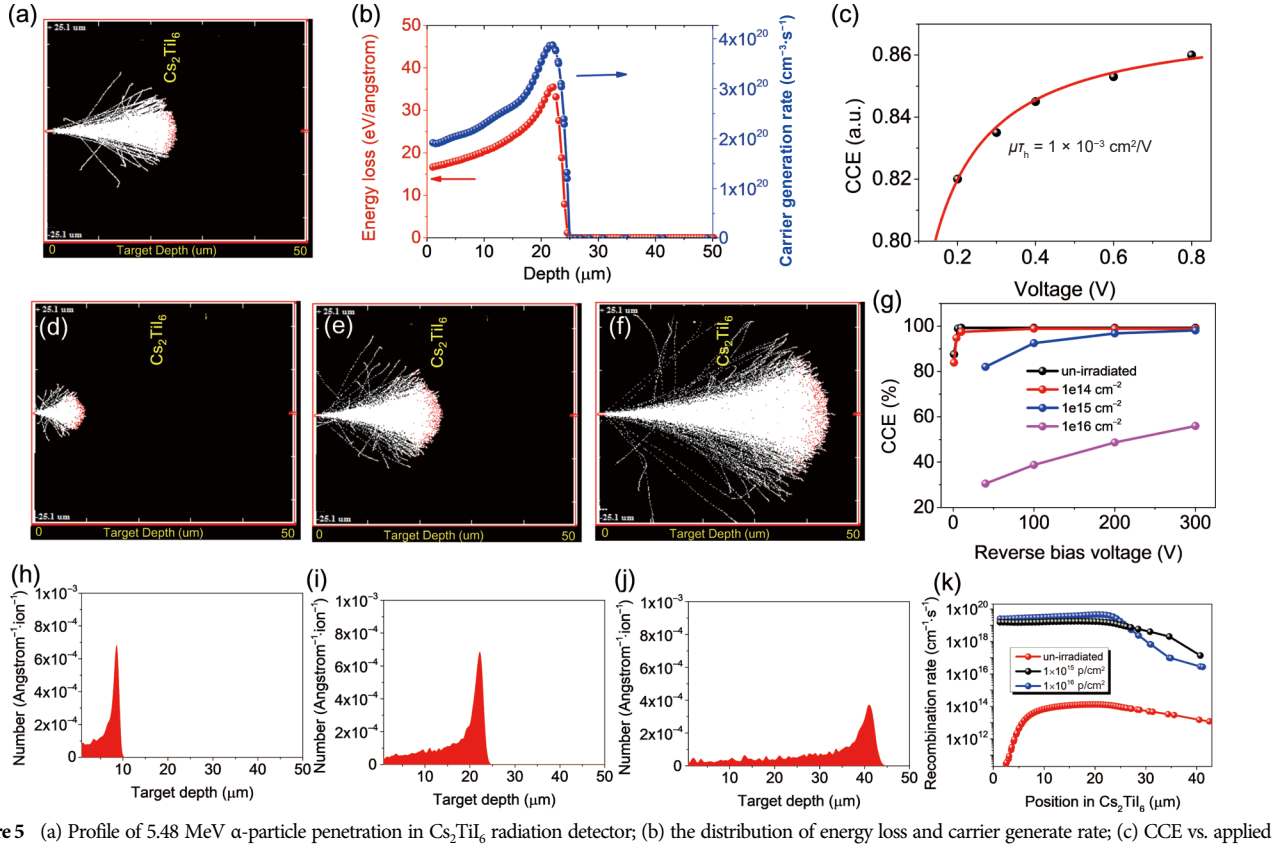

Figure 5 (a) Profile of 5.48 MeV α-particle penetration in Cs_2TiI_6 radiation detector; (b) the distribution of energy loss and carrier generate rate; (c) CCE vs. applied voltage fitting with Hecht equation. Profile of (d) 0.7 MeV, (e) 1.32 MeV, (f) 2 MeV proton penetration in the Cs_2TiI_6 radiation detector; (g) CCE vs. applied voltage with different proton fluences; the distribution of vacancies when the Cs_2TiI_6 radiation detector is bombarded by proton with energy of (h) 0.7 MeV, (i) 1.32 MeV, (j) 2 MeV; (k) recombination rate with different proton fluences.

linear energy transfer increase near the end of particle penetration, which induces the improvement of carrier generation rate (Fig. 5(b)). As the most important parameter in α-particle detection, the mobility-lifetime product $\mu\tau_h$ is calculated by the Hecht equation, as displayed in Fig. 5(c). The ultrahigh $\mu\tau_h$ product with 1×10^{-3} cm^2/V is achieved by the Cs_2TiI_6 material, which is superior to the $CsPbBr_3$ α-particle detector (9.5×10^{-4} cm^2/V) and several orders of magnitude higher than that of two-dimensional perovskites α-particle detector ($Cs_3Bi_2I_9$: 1.8×10^{-5} cm^2/V, $Rb_3Bi_2I_9$: 2×10^{-6} cm^2/V) [28, 51]. In addition, in order to access the radiation resistance, the effect of proton damage in Cs_2TiI_6 α-particle detector is investigated as well, as displayed in Figs. 5(d)–5(k). It is obviously observed that the most vacancies concentrate in the position of 23 μm with 1.32 MeV proton beam. Meanwhile, the highest carrier generation rate locates in the position of 23 μm as well. Therefore, 1.32 MeV proton energy will induce the most serious damage in the device and is selected for the following analysis. As shown in Fig. 5(g), owing to the larger mass density and excellent carrier mobility of Cs_2TiI_6 material, the ultrahigh CCE of 99.2% can be obtained by the pre-irradiated device, much higher than the reported $CsPbBr_3$ α-particle detector (95.2%) [51]. It indicates that the Cs_2TiI_6 material has broad prospect in radiation detection. Such ultrahigh CCE can remain even if the high fluence proton beam increases to 10^{14} p/cm^2. Moreover, even though increasing the proton fluence to 10^{15} p/cm^2, the ultrahigh CCE just reduces 1.2% under the applied voltage of 300 V. Only when continuously increasing the proton fluence to 10^{16} p/cm^2, the obvious detector performance deterioration can be observed due to the significant increment of carrier recombination rate (Fig. 5(k)). However, the CCE still can be up to 55.9%. It suggests that Cs_2TiI_6 α-particle detector possessed the superior radiation tolerance can resist the bombardment of high fluence proton beam (10^{15} p/cm^2) which is about one order of magnitude higher radiation tolerance than the 4H-SiC (10^{14} p/cm^2) and GaAs (1.6×10^{14} p/cm^2) radiation detector reported in the literature [52, 53]. Therefore, owing to the excellent material properties, device performance, and radiation tolerance, the novel vacancy-ordered double perovskite Cs_2TiI_6 is suitable to be employed as α-particle detector and even other radiation detections.

4 Conclusion

In summary, a nontoxic and stable vacancy-ordered double perovskite Cs_2TiI_6 used for high-performance solar cell and α-particle detector is investigated. The superior optical absorption property and high carrier mobility obtained from first-principle calculation make it suitable to apply in photovoltaic cells and radiation detection. The further device and radiation simulation suggests that the ideal materials properties can be transferred into the device level successfully. The ultrahigh PCE (22.70%) of Cs_2TiI_6 single junction solar cell can be realized with 50 nm ultrathin active layer. Similarly, the PCE of monolithic all-perovskite tandem solar cell with ultrathin absorbed layer ($MAPbI_3$ = 186 nm, Cs_2TiI_6 = 70 nm) can reach up to 26.87% as well. Meanwhile, the single junction Cs_2TiI_6 solar cell can still retain over 95% of the initial PCE even after proton irradiation with the fluence of 10^{13} p/cm^2. In addition, owing to the excellent carrier mobility, the ultrahigh CCE (99.2%) and superior mobility-lifetime product ($\mu\tau_h = 1\times10^{-3}$ cm^2/V) can be realized by α-particle detector based on Cs_2TiI_6 material, furthermore, it can survive against accumulated proton fluence level up to 10^{15} p/cm^2. We expect that this study can accelerate the experiment of preparing and testing photovoltaic cells and radiation detectors based on Cs_2TiI_6 material.

Acknowledgements

This work was financially supported by the National Natural Science Foundation of China (Nos. 61704131, 61804111, and 11435010), Key Research and Development Program of Shaanxi Province (No. 2020GY-310), the Fundamental Research Funds for the Central Universities, the Innovation Fund of Xidian University, Initiative Postdocs Supporting Program (No. BX20180234), Project funded by China Postdoctoral Science Foundation (No. 2018M643578). The numerical calculations in this paper were done on the HPC system of Xidian University.

Electronic Supplementary Material: Supplementary material (the following parts: (1) incident and reflect light interference effect (Figure S1); (2) influence of carrier mobility (Figure S2), carrier lifetime (Figure S3) and defect energy level (Figure S4); device structures (Figure S5); proton penetration with 230 nm Cs_2TiI_6 layer (Figure S6), 420 nm Cs_2TiI_6 layer (Figure S7) and 300 nm $MAPbI_3$ layer (Figure S8); parameters of Cs_2TiI_6, $MAPbI_3$, C_{60} and PEDOT:PSS (Table S1-S2)) is available in the online version of this article at https://doi.org/10.1007/s12274-021-3801-5.

References

[1] Ma, J.; Su, J.; Lin, Z. H.; Zhou, L.; He, J.; Zhang, J. C.; Liu, S. Z.; Chang, J.; Hao, Y. Improve the oxide/perovskite heterojunction contact for low temperature high efficiency and stable all-inorganic $CsPbI_2Br$ perovskite solar cells. *Nano Energy* **2020**, *67*, 104241.

[2] Dohner, E. R.; Jaffe, A.; Bradshaw, L. R.; Karunadasa, H. I. Intrinsic white-light emission from layered hybrid perovskites. *J. Am. Chem. Soc.* **2014**, *136*, 13154–13157.

[3] Leung, S. F.; Ho, K. T.; Kung, P. K.; Hsiao, V. K. S.; Alshareef, H. N.; Wang, Z. L.; He, J. H. A self-powered and flexible organometallic halide perovskite photodetector with very high detectivity. *Adv. Mater.* **2018**, *30*, 1704611.

[4] Di, J. Y.; Du, J. H.; Lin, Z. H.; Liu S. Z.; Ouyang, J. Y.; Chang, J. J. Recent advances in resistive random access memory based on lead halide perovskite. *InfoMat* **2021**, *3*, 293–315.

[5] Senanayak, S. P.; Yang, B. Y.; Thomas, T. H.; Giesbrecht, N.; Huang, W. C.; Gann, E.; Nair, B.; Goedel, K.; Guha, S.; Moya, X. et al. Understanding charge transport in lead iodide perovskite thin-film field-effect transistors. *Sci. Adv.* **2017**, *3*, e1601935.

[6] Xu, L.; Xiong, Y.; Mei, A. Y.; Hu, Y.; Rong, Y. G.; Zhou, Y. H.; Hu, B.; Han, H. W. Efficient perovskite photovoltaic-thermoelectric hybrid device. *Adv. Energy Mater.* **2018**, *8*, 1702937.

[7] Zhang, Y. X.; Liu, Y. C.; Xu, Z.; Ye, H. C.; Yang, Z.; You, J. X.; Liu, M.; He, Y. H.; Kanatzidis, M. G.; Liu, S. Z. Nucleation-controlled growth of superior lead-free perovskite $Cs_3Bi_2I_9$ single-crystals for high-performance X-ray detection. *Nat. Commun.* **2020**, *11*, 2304.

[8] Xu, Q.; Wei, H. T.; Wei, W.; Chuirazzi, W.; DeSantis, D.; Huang, J. S.; Cao, L. Detection of charged particles with a methylammonium lead tribromide perovskite single crystal. *Nucl. Instrum. Methods Phys. Res. Sect. A Accel. Spectrom., Detect. Assoc. Equip.* **2017**, *848*, 106–108.

[9] Barbé, J.; Hughes, D.; Wei, Z. F.; Pockett, A.; Lee, H. K. H.; Heasman, K. C.; Carnie, M. J.; Watson, T. M.; Tsoi, W. C. Radiation hardness of perovskite solar cells based on aluminum-doped zinc oxide electrode under proton irradiation. *Sol. RRL* **2019**, *3*, 1900219.

[10] Malinkiewicz, O.; Imaizumi, M.; Sapkota, S. B.; Ohshima, T.; Ö z, S. Radiation effects on the performance of flexible perovskite solar cells for space applications. *Emergent Mater.* **2020**, *3*, 9–14.

[11] Lang, F.; Nickel, N. H.; Bundesmann, J.; Seidel, S.; Denker, A.; Albrecht, S.; Brus, V. V.; Rappich, J.; Rech, B.; Landi, G. et al. Radiation hardness and self-healing of perovskite solar cells. *Adv. Mater.* **2016**, *28*, 8726–8731.

[12] Lang, F.; Jošt, M.; Bundesmann, J.; Denker, A.; Albrecht, S.; Landi, G.; Neitzert, H. C.; Rappich, J.; Nickel, N. H. Efficient minority carrier detrapping mediating the radiation hardness of triple-cation

perovskite solar cells under proton irradiation. *Energy Environ. Sci.* **2019**, *12*, 1634–1647.

[13] Lang, F.; Jošt, M.; Frohna, K.; Köhnen, E.; Al-Ashouri, A.; Bowman, A. R.; Bertram, T.; Morales-Vilches, A. B.; Koushik, D.; Tennyson, E. M. et al. Proton radiation hardness of perovskite tandem photovoltaics. *Joule* **2020**, *4*, 1054–1069.

[14] Babayigit, A.; Ethirajan, A.; Muller, M.; Conings, B. Toxicity of organometal halide perovskite solar cells. *Nat. Mater.* **2016**, *15*, 247–251.

[15] Giustino, F.; Snaith, H. J. Toward lead-free perovskite solar cells. *ACS Energy Lett.* **2016**, *1*, 1233–1240.

[16] Di, J. Y.; Chang, J. J.; Liu, S. Z. Recent progress of two-dimensional lead halide perovskite single crystals: Crystal growth, physical properties, and device applications. *EcoMat* **2020**, *2*, e12036.

[17] Leijtens, T.; Bush, K.; Cheacharoen, R.; Beal, R.; Bowring, A.; McGehee, M. D. Towards enabling stable lead halide perovskite solar cells; Interplay between structural, environmental, and thermal stability. *J. Mater. Chem. A* **2017**, *5*, 11483–11500.

[18] Li, Z.; Yang, M. J.; Park, J. S.; Wei, S. H.; Berry, J. J.; Zhu, K. Stabilizing perovskite structures by tuning tolerance factor: Formation of formamidinium and cesium lead iodide solid-state alloys. *Chem. Mater.* **2016**, *28*, 284–292.

[19] Pantaler, M.; Cho, K. T.; Queloz, V. I.; Benito,I. G.; Fettkenhauer, C.; Anusca, I.; Nazeeruddin, M. K.; Lupascu, D. C.; Grancini, G. Hyteresis-free lead-free double-perovskite solar cells by interface engineering. *ACS Energy Lett.* **2018**, *3*, 1781–1786.

[20] Volonakis, G.; Haghighirad, A. A.; Milot, R. L.; Sio, W. H.; Filip, M. R.; Wenger, B.; Johnston, M. B.; Herz, L. M.; Snaith, H. J.; Giustino, F. $Cs_2InAgCl_6$: A new lead-free halide double perovskite with direct band gap. *J. Phys. Chem. Lett.* **2017**, *8*, 772–778.

[21] Zhang, H.; Su, J.; Hou, J.; Lin, Z. H.; Hu, Z. S.; Chang, J. J.; Zhang, J. C.; Hao, Y. Potential applications of halide double perovskite Cs_2AgInX_6 (X = Cl, Br) in flexible optoelectronics: Unusual effects of uniaxial strains. *J. Phys. Chem. Lett.* **2019**, *10*, 1120–1125.

[22] Park, B. W.; Philippe, B.; Zhang, X. L.; Rensmo, H.; Boschloo, G.; Johansson, E. M. J. Bismuth based hybrid perovskites $A_3Bi_2I_9$ (A: Methylammonium or Cesium) for solar cell application. *Adv. Mater.* **2015**, *27*, 6806–6813.

[23] Ju, M. G.; Dai, J.; Ma, L.; Zeng, X. C. Lead-free mixed tin and germanium perovskites for photovoltaic application. *J. Am. Chem. Soc.* **2017**, *139*, 8038–8043.

[24] Greul, E.; Petrus, M. L.; Binek, A.; Docampo, P.; Bein, T. Highly stable, phase pure $Cs_2AgBiBr_6$ double perovskite thin films for optoelectronic applications. *J. Mater. Chem. A* **2017**, *5*, 19972–19981.

[25] Gao, W. Y.; Ran, C. X.; Xi, J.; Jiao, B.; Zhang, W. W.; Wu, M. C.; Hou, X.; Wu, Z. X. High-quality $Cs_2AgBiBr_6$ double perovskite film for lead-free inverted planar heterojunction solar cells with 2.2% efficiency. *ChemPhysChem* **2018**, *19*, 1696–1700.

[26] Qiu, X. F.; Jiang, Y. N.; Zhang, H. L.; Qiu, Z. W.; Yuan, S.; Wang, P.; Cao, B. Q. Lead-free mesoscopic Cs_2SnI_6 perovskite solar cells using different nanostructured ZnO nanorods as electron transport layers. *Phys. Status Solidi* **2016**, *10*, 587–591.

[27] Chen, M.; Ju, M. G.; Carl, A. D.; Zong, Y. X.; Grimm, R. L.; Gu, J. J.; Zeng, X. C.; Zhou, Y. Y.; Padture, N. P. Cesium titanium(IV) bromide thin films based stable lead-free perovskite solar cells. *Joule* **2018**, *2*, 558–570.

[28] McCall, K. M.; Liu, Z. F.; Trimarchi, G.; Stoumpos, C. C.; Lin, W. W.; He, Y. H.; Hadar, I.; Kanatzidis, M. G.; Wessels, B. W. α-particle detection and charge transport characteristics in the $A_3M_2I_9$ defect perovskites (A = Cs, Rb; M = Bi, Sb) . *ACS Photonics* **2018**, *5*, 3748–3762.

[29] Kresse, G.; Furthmüller, J. Efficient iterative schemes for *ab initio* total-energy calculations using a plane-wave basis set. *Phys. Rev. B.* **1996**, *54*, 11169–11186.

[30] Perdew, J. P.; Burke, K.; Ernzerhof, M. Generalized gradient approximation made simple. *Phys. Rev. Lett.* **1996**, *77*, 3865–3868.

[31] Zhao, P.; Liu, Z. Y.; Lin, Z. H.; Chen, D. Z.; Su, J.; Zhang, C. F.; Zhang, J. C.; Chang, J. J.; Hao, Y. Device simulation of inverted $CH_3NH_3PbI_{3-x}Cl_x$ perovskite solar cells based on PCBM electron transport layer and NiO hole transport layer. *Sol. Energy* **2018**, *169*, 11–18.

[32] Zhao, P.; Lin, Z. H.; Wang, J. P.; Yue, M.; Su, J.; Zhang, J. C.; Chang, J. J.; Hao, Y. Numerical simulation of planar heterojunction perovskite solar cells based on SnO_2 electron transport layer. *ACS Appl. Energy Mater.* **2019**, *2*, 4504–4512.

[33] Zhao, P.; Feng, L. P.; Lin, Z. H.; Wang, J. P.; Su, J.; Hu, Z. S.; Zhang, J. C.; Ouyang, X. P.; Chang, J. J.; Hao, Y. Theoretical analysis of two-terminal and four-terminal perovskite/copper indium gallium selenide tandem solar cells. *Sol. RRL* **2019**, *3*, 1900303.

[34] Zhao, P.; Su, J.; Lin, Z. H.; Wang, J. P.; Zhang, J. C.; Hao, Y.; Ouyang, X. P.; Chang, J. J. The crystal anisotropy effect of $MAPbI_3$ perovskite on optoelectronic devices. *Mater. Today Energy* **2020**, *17*, 100481.

[35] Zhao, P.; Su, J.; Lin, Z. H.; Wang, J. P.; Zhang, J. C.; Hao, Y.; Ouyang, X. P.; Chang, J. J. All-inorganic $CsPbI_xBr_{3-x}$ perovskite solar cells: Crystal anisotropy effect. *Adv. Theory Simul.* **2020**, *3*, 2000055.

[36] Conway, A. M.; Wang, T. F.; Deo, N.; Cheung, C. L.; Nikolić, R. J. Numerical simulations of pillar structured solid state thermal neutron detector: Efficiency and gamma discrimination. *IEEE Trans. Nucl. Sci.* **2009**, *56*, 2802–2807.

[37] Tsai, H.; Nie, W. Y.; Blancon, J. C.; Stoumpos, C. C.; Asadpour, R.; Harutyunyan, B.; Neukirch, A. J.; Verduzco, R.; Crochet, J. J.; Tretiak, S. et al. High-efficiency two-dimensional Ruddlesden–Popper perovskite solar cells. *Nature* **2016**, *536*, 312–316.

[38] Zhao, P.; Yue, M.; Lei, C.; Lin, Z. H.; Su, J.; Chen, D. Z.; Zhang, C. F.; Zhang, J. C.; Chang, J. J.; Hao, Y. Device simulation of organic–inorganic halide perovskite/crystalline silicon four-terminal tandem solar cell with various antireflection materials. *IEEE J. Photovolt.* **2018**, *8*, 1685–1691.

[39] Dong, Q. F.; Fang, Y. J.; Shao, Y. C.; Mulligan, P.; Qiu, J.; Cao, L.; Huang, J. S. Electron-hole diffusion lengths > 175 mm in solution-grown $CH_3NH_3PbI_3$ single crystals. *Science* **2015**, *347*, 967–970.

[40] Minemoto, T.; Kawano, Y.; Nishimura, T.; Shen, Q.; Yoshino, K.; Iikubo, S.; Hayase, S.; Chantana, J. Theoretical analysis of band alignment at back junction in Sn–Ge perovskite solar cells with inverted p-i-n structure. *Sol. Energy Mater. Sol. Cells* **2020**, *206*, 110268.

[41] Frankevich, E.; Maruyama, Y.; Ogata, H. Mobility of charge carriers in vapor-phase grown C_{60} single crystal. *Chem. Phys. Lett.* **1993**, *214*, 39–44.

[42] Chelliah, C. R. A. J.; Szymanik, B.; Swaminathan, R. Study of electron transport in fullerene (C_{60}) quantum confined channel layer based field effect transistor. *Int. J. Adv. Eng. Res. Sci.* **2017**, *4*, 119–125.

[43] Peumans, P.; Forrest, S. R. Very-high-efficiency double-heterostructure copper phthalocyanine/C_{60} photovoltaic cells. *Appl. Phys. Lett.* **2001**, *79*, 126–128.

[44] Ye, F.; Lin, H.; Wu, H. D.; Zhu, L.; Huang, Z. F.; Ouyang, D.; Niu, G. D.; Choy, W. C. H. High-quality cuboid $CH_3NH_3PbI_3$ single crystals for high performance X-ray and photon detectors. *Adv. Funct. Mater.* **2019**, *29*, 1806984.

[45] Brendel, W.; Samartzis, T.; Brendel, C.; Krebs, B. TG and DTA investigations on hexaiodometallates. *Thermochim. Acta* **1985**, *83*, 167–172.

[46] Debbichi, L.; Lee, S.; Cho, H.; Rappe, A. M.; Hong, K. H.; Jang, M. S.; Kim, H. Mixed valence perovskite $Cs_2Au_2I_6$: A potential material for thin-film Pb-free photovoltaic cells with ultrahigh efficiency. *Adv. Mater.* **2018**, *30*, 1707001.

[47] Ahmed, S.; Jannat, F.; Khan, M. A. K.; Alim, M. A. Numerical development of eco-friendly Cs_2TiBr_6 based perovskite solar cell with all-inorganic charge transport materials via SCAPS-1D. *Optik* **2021**, *225*, 165765.

[48] Lin, R. X.; Xiao, K.; Qin, Z. Y.; Han, Q. L.; Zhang, C. F.; Wei, M. Y.; Saidaminov, M. I.; Gao, Y.; Xu, J.; Xiao, M. et al. Monolithic all-perovskite tandem solar cells with 24.8% efficiency exploiting comproportionation to suppress Sn(II) oxidation in precursor ink. *Nat. Energy* **2019**, *4*, 864–873.

[49] Morita, Y.; Ohshima, T.; Nashiyama, I.; Yamamoto, Y.; Kawasaki, O.; Matsuda, S. Anomalous degradation in silicon solar cells subjected to high-fluence proton and electron irradiations. *J. Appl. Phys.* **1997**, *81*, 6491–6493.

[50] Ohshima, T.; Sato, S. I.; Nakamura, T.; Imaizumi, M.; Sugaya, T.; Matsubara, K.; Niki, S.; Takeda, A.; Okano, Y. Electrical performance degradation of GaAs solar cells with InGaAs quantum dot layers due to proton irradiation. In *2013 IEEE 39th Photovoltaic Specialists Conference (PVSC)*, Tampa, 2013, pp 2779–2783.

[51] He, Y. H.; Liu, Z. F.; McCall, K. M.; Lin, W. W.; Chung, D. Y.; Wessels, B. W.; Kanatzidis, M. G. Perovskite $CsPbBr_3$ single crystal detector for alpha-particle spectroscopy. *Nucl. Instrum. Methods Phys. Res. Sect. A Accel. Spectrom., Detect. Assoc. Equip.* **2019**, *922*, 217–221.

[52] Nava, F.; Vittone, E.; Vanni, P.; Fuochi, P. G.; Lanzieri, C. Radiation tolerance of epitaxial silicon carbide detectors for electrons and γ-rays. *Nucl. Instrum. Methods Phys. Res. Sect. A Accel. Spectrom., Detect. Assoc. Equip.* **2003**, *514*, 126–134.

[53] Nava, F.; Vanni, P.; Canali, C.; Apostolo, G.; Manfredotti, C.; Polesello, P.; Vittone, E. Analysis of uniformity of as prepared and irradiated S.I. GaAs radiation detectors. *IEEE Trans. Nucl. Sci.* **1998**, *45*, 609–616.